EES Batteries

PAPER

View Article Online
View Journal

Cite this: DOI: 10.1039/d6eb00002a

Scaling up Si–C composite synthesis from recycled graphite for high-energy density and low-environmental impact batteries

Denis Dienguila Kionga, [a] Théodore Barret,[a] Martin Raaen,[a] Lisa Vericel,[b] Anna Vanderbruggen, [c] Giulia Pezzin, [d] Giovanni Andrea Blengini, [d] Alessandra Manzini, [e] Willy Porcher [b] and Pascale Chenevier *[a]

Received 7th January 2026,
Accepted 12th May 2026

DOI: 10.1039/d6eb00002a

rsc.li/EESBatteries

Graphite-silicon (GtSi) composites are recognized as promising materials as a replacement of graphite in lithium battery anodes because of their high specific capacity of around 1000 mAh g^{-1} and their mitigated volume change in cycling. Taking advantage of the recent progress in used battery treatment, we investigate the production of GtSi from recycled graphite as a strategy for material upcycling. The present paper reports the scaling-up of GtSi synthesis to a 25 gram scale. To manage the risk associated with this growth process involving pyrophoric reagents and hydrogen gas evolution at 400 °C under 10 bar, the kinetic and thermodynamic parameters of diphenylsilane thermal decomposition were accurately measured. The scaled-up synthesis of GtSi then allowed the use of relevant roll-to-roll battery electrode fabrication and assembly of 40 mAh GtSi|NMC811 pouch cells and demonstrated a high energy density of 984 Wh L^{-1}. Finally, life cycle assessment has been used to identify environmental hotspots for GtSi and GtSi|NMC cell fabrication. Lab-scale primary data were used to draw transparent and clear life cycle inventories, thus contributing to filling data gaps, typically a bottleneck in LCAs of novel battery materials and technologies.

Broader context

To meet their promise of a more sustainable world, electric mobility systems must adopt a circular economy perspective. This requires that batteries not only be recyclable but also include an increasing proportion of recycled raw materials. However, recycling adds up to costs, and recycled raw materials exhibit lower purity, which often translates into lower performance. The present paper proposes upgrading graphite recycled from anodes of used batteries into a more energy-dense anode material for next-generation batteries. The experimental study is completed by a life cycle analysis, showing the environmental relevance of this approach.

Introduction

Silicon (Si) is a highly promising material for lithium-ion battery (LIB) anodes[1] due to its exceptional theoretical capacity of 3579 mAh g^{-1}, corresponding to the uptake of 3.75 Li per Si atom. However, this high capacity is accompanied by a large volume expansion of 280% during lithiation, which challenges cycling stability. Nanostructuration of Si proved to be effective in overcoming this issue and demonstrating both high anode capacity and long cycling stability.[2] A wide literature on Si nanoparticles, nanowires and nanocomposites has reported decades of improvements in high-energy density LIB anode materials compatible with several technologies of LIBs,[3–7] including Li–S[8,9] and solid-state batteries.[10–13] However, it mostly deals with the synthesis of small batches of a few 100 mg of material, which in turn restricts the electrochemical tests to lab-scale LIB cells.

Electrode formulation and fabrication can offer much higher quality electrodes based on appropriate ink mixing and continuous electrode coating. LIB fabrication by a roll-to-roll process gives access to more reliable battery tests and a more detailed understanding of material behavior. The refined design of the slurry and roll-to-roll electrode fabrication require quantities of materials on the 20–100 gram scale, a challenge in nanomaterial synthesis in general and in nano-silicon in particular. Scaling-up material synthesis requires

[a]Univ. Grenoble Alpes, CEA, CNRS, Grenoble-INP, IRIG, SYMMES, 38000 Grenoble, France. E-mail: pascale.chenevier@cea.fr
[b]Univ. Grenoble Alpes, CEA, LITEN, DEHT, 38000 Grenoble, France
[c]Université de Lorraine, CNRS, GeoRessources, F-54506 Vandoeuvre-lès-Nancy, France
[d]Politecnico di Torino, Torino, Italy
[e]CY Paris University, Cergy, France

taking into account cost, yield and safety issues, which are often postponed in early-stage studies by reducing the amount of matter to be handled. Yet considering such issues gives meaningful information to forecast opportunities and barriers on the way to possible industrialization, including for a first life cycle analysis. Here, we report on the scale-up of active material synthesis to above 25 grams for this purpose.

Graphite-silicon (GtSi) composites showed interesting performance in high-energy density LIBs in the literature[14–18] and our previous studies.[19,20] We demonstrated that the anode volume change due to silicon lithiation was mitigated by its composition with graphite. GtSi with 20% Si in weight afforded a capacity above 1000 mAh g^{-1}, although compliant with an industrially relevant areal capacity of 4 mAh cm^{-2}. In this work, we replace battery-grade graphite by graphite recycled from used batteries in the synthesis of a more sustainable GtSi.

The European Union's new Batteries Regulation (EU 2023/1542) sets recycling efficiency targets for lithium-based batteries: 65% by mass by 2025, increasing to 70% by 2030. These targets highlight the strategic importance of recovering valuable battery materials, making the recycling of graphite from spent LIBs a critical objective for sustainable and resilient battery supply chains in Europe. While recycling the metal oxides from LIB cathode materials offers an economically viable way in providing a high-value product,[21] graphite recycling faces a more difficult challenge due to its relatively low economic value. At the same time, the escalating global demand for LIBs is driving significant growth in the graphite anode market, projected to increase[22] from USD 9.2 billion in 2023 to USD 29.9 billion by 2033, highlighting the need for sustainable resource management. Efficient recovery of graphite from spent LIBs is therefore essential both for maintaining the supply of this key material and for supporting industrial-scale battery production in an environmentally sustainable way.

Graphite can be efficiently recovered from the black mass of spent LIBs and cell scraps using techniques such as froth flotation combined with thermal pre-treatment (*e.g.*, pyrolysis), which can yield a high-purity material and separated carbon suitable for reuse.[23] These recycling processes provide an economically and environmentally competitive alternative to relying on natural graphite resources from primary producers like Mozambique, Madagascar, and Brazil.[24] Operations in these territories often have a high level of impact on the human rights of Indigenous Peoples and Local Communities (IPLCs), as exemplified by ongoing security issues and social unrest.[25,26] Overall, this circular approach not only supports the circular economy by integrating refined carbon materials back into the production of next-generation energy devices, potentially increasing their adoption appeal,[27] but also provides a cost-effective solution. Here, graphite recycled by froth flotation was used. It was demonstrated that, after a high temperature refinement, this material can deliver a capacity similar to novel graphite when implemented in LIBs.[28,29] Refurbished into a composite with silicon, it attains a much higher specific capacity, which opens an attractive pathway back into the battery value chain.

This study includes a scale-up of the synthesis to attain 25 g per batch in a safe and controlled lab process. Industrial scale-ups of nano-silicon synthesis of battery materials have been reported based on SiH_4 as the Si source. The present study led at a lab scale uses diphenylsilane as a safer silane surrogate[30–33] and reports on the associated yield optimization and safety issues. The chemical dynamics of diphenylsilane thermolysis, as well as that of phenylsilane and triphenylsilane, which are reaction intermediates, was carefully studied and rate and equilibrium constants were measured to allow forecasting safe silicon growth conditions. This chemical dynamic study will eventually be useful in designing other silicon chemical deposition processes.

The scale-up was performed using both recycled graphite and new battery-grade graphite for comparison, yielding the composites denoted as R-GtSi and n-GtSi, respectively. Then R-GtSi and n-GtSi are processed for the first time on a roll-to-roll electrode fabrication line and tested in GtSi|NMC811 cells of high energy density with 984 Wh L^{-1} after assembly considering the cell electrochemical core. Finally, life-cycle assessment of anode fabrication and full-cell assembly provides a quantitative evaluation of the environmental impact associated with this scalable and circular material strategy.

Materials and methods

Chemicals

Diphenylsilane was purchased from Chemical Point. Tin chloride hydrate (98%) was purchased from Strem Chemicals. Phenylsilane and triphenylsilane were purchased from Sigma-Aldrich. Solvents *N*-methylpyrrolidone (NMP), ethanol, and acetone were purchased from Sigma-Aldrich or Carlo Erba.

Kinetic study of the disproportionation of phenylsilanes by ^{1}H-NMR

Pure diphenylsilane (200 μL), phenylsilane (200 μL) or triphenylsilane (280 μL) was sealed in 30 mL borosilicate glass tubes under vacuum. The quantity was chosen to produce an internal pressure of about 3 bar in the glass tube once the organosilane evaporates at high temperature, a pressure relevant to conditions at the beginning of GtSi synthesis. The tubes were heated in a tubular furnace (Carbolite Gero) at 300 °C or 400 °C. After cooling, the tubes were opened by breaking the glass with a hammer in a sealed plastic bag to avoid projection of broken glass under possible pressure. The product was solubilized in deuterated chloroform and analyzed by ^{1}H-NMR using a 400 MHz Advance Neo spectrometer (Bruker). The longest proton relaxation rate of these samples was measured and the T_1 relaxation time was set to 30 s to record quantitative spectra. The ratio of $PhSiH_3$, Ph_2SiH_2 and Ph_3SiH concentrations was determined through the integrated intensity of their characteristic Si–H peaks (Fig. S1), and the concentration of PH_4Si was deduced from the aromatic peaks after subtraction of the expected intensity from the $PhSiH_3$, Ph_2SiH_2 and Ph_3SiH aromatic protons. A small amount of

benzene was detected in samples after prolonged heating time.[34] SiH_4 could not be recovered but was detected in some glass tubes through the internal pressure at the opening and the deposition of fine white silica powder at the opening edge. Its amount was calculated using the mass conservation law.

Synthesis of graphite-silicon composites

Graphite SLP30 (Imerys) was used as new graphite. Recycled graphite was prepared as described in the previous work.[28] Tin sulfide nanoparticles were deposited on graphite following a method adapted by Zhu *et al.*[35] Graphite (new or recycled, 25 g) was dispersed in ethanol (25 mL) and then diluted with distilled water (100 mL) under stirring for 10 minutes. The graphite suspension was slowly added to a solution of tin chloride ($SnCl_2{\cdot}2H_2O$, 10 mmol in 150 mL of distilled water) at 85 °C under vigorous stirring. A solution of thioacetamide (C_2H_5NS, 10 mmol in 25 mL of distilled water) was then added and the reaction was allowed to proceed for 2 hours. Finally, the reaction mixture was filtered and the SnS-graphite powder was washed with distilled water and acetone and dried in air at 100 °C for 10 minutes.

The SnS-graphite powder was introduced on aluminum foil shells in a steel pressure reactor in a closed or half-open configuration, with diphenylsilane under primary vacuum. The steel reactors, certified for 30 bar operation, have 7 mm thick walls and are heated using a 1.2 kW resistive cylindrical oven with temperature control (Equilabo, France). They are equipped with a safety valve, a plunging J-type thermocouple and a pressure sensor (Wika, Germany) with continuous recording. The closed reactor derived from our previous design[19] has an inner chamber volume of 150 mL and was loaded with up to 12 mL of diphenylsilane and 1 g of SnS-graphite. It was operated at a constant temperature until a pressure of 20 bar was attained. The half-open reactor (Fig. S2) has an inner chamber volume of 300 mL topped with a 40 cm-high cooling column and a tunable spillway (Parr, USA) and was loaded with up to 100 mL of diphenylsilane and 20 g of SnS-graphite. It was heated either at constant temperature or following a slow temperature ramp. After growth and cooling down, the valve was carefully opened in the hood to let excess gas slowly escape. Then the reactor was opened and the recovered powder was washed with acetone, ground in a mortar, washed again with acetone and dichloromethane and dried in air at 120 °C for 10 minutes.

Material characterization

Scanning electron microscopy (SEM) was performed using a Zeiss Ultra 55+ microscope at an accelerating voltage of 5 kV and a working distance of 5 mm. For elemental analysis, 2 mg of GtSi composite was pressed into a 5 mm-diameter pellet in a hydraulic press (Specac) under 2 tons of pressure for 2 min to obtain a dense sample (>85%) with a flat surface. Energy-dispersive X-ray spectroscopy (EDX) spectra were recorded using the same SEM microscope at an accelerating voltage of 10 kV at a working distance of 7 mm. The apparatus was first calibrated with a series of elemental standards (Zeiss). Powder X-ray diffraction has been carried out using a D8 Discover powder diffractometer equipped with a copper anode (Kα1 = 1.5406 Å; Kα2 = 1.5444 Å) and a 1D LynxEye XE-T detector. It was configured in Bragg–Brentano geometry, with a variable divergence slit on the primary beam path and a set of antiscattering slits positioned before the sample. Axial divergence was limited by 2.5 deg Soller slits. Data analysis (Le Bail profile refinements) was performed using HighScorePlus software.

Electrochemical tests in batteries

The negative electrode is composed of 90 wt% of graphite-silicon composites (n-GtSi or R-GtSi), 3 wt% of carbon black (CB from Imerys, SuperP C65), 1 wt% of vapor-grown carbon fibers (VGCFs from Showa Denko), 0.2 wt% of single-wall carbon nanotubes (OcSiAl), 3.2 wt% of sodium carboxymethyl cellulose (Na-CMC from Ashland) and 2.6 wt% of latex (TRD302A from Eneos). The slurry was dispersed in DI water for 40 min using a Dispermat® and refined with a three-roll mill (Exakt) until a quality of dispersion of D_{100} < 50 μm was obtained. The slurry was then coated on a 10 μm-thick copper current collector foil with a loading of 4.5 mg cm^{-2} using a roll-to-roll coating machine with a comma-bar coating head. Then, the electrode was pressed down to a thickness of 44 μm including the current collector using a rolling press machine to reach a porosity of 35%.

The positive electrode is composed of 96 wt% of NMC811 (Targray), 2 wt% of binder (Solvay 5130 PVDF), 1.5 wt% of CB and 0.5 wt% of VGCF. The slurry was dispersed in NMP for 25 min using a Dispermat® and was then coated on a 20 μm-thick aluminum current collector foil with a loading of 21 mg cm^{-2} using a roll-to-roll coating machine with a comma-bar coating head. Then, the electrode was pressed down to a thickness of 85 μm including the current collector using a rolling press machine to reach a porosity of 30%.

For the preparation of coin cells (CR2032), negative electrode discs (∅14 mm) were cut out of electrode rolls and dried overnight at 105 °C in order to remove residual water. Coin cells were assembled in a glove box filled with an argon atmosphere, using lithium foil as an anode (Sigma-Aldrich, 99.99% purity, 135 μm thick, disc of 16 mm diameter) and Celgard 2400 as a separator. The electrolyte was composed of 1 M $LiPF_6$ (Sigma-Aldrich, 99.99% purity) in a mixture of ethylene carbonate (EC), dimethyl carbonate (DMC) and ethyl methyl carbonate (EMC), 2 : 5 : 3 by volume with 10 wt% of fluoroethylene carbonate (FEC) and 2 wt% of vinylene carbonate (VC).

Single layer pouch (SLP) cells with a square shape of 10.2 cm^2 for the positive electrode were also assembled with the graphite-silicon composite negative electrodes and a Celgard 2320 separator in a dry room after secondary drying of the electrodes. The SLP cells were then introduced in a glove box to be filled with the same electrolyte as coin cells and sealed under vacuum.

The energy density of the cell electrochemical core was calculated considering the reversible capacity during the first cycle, the active surface of the cathode, the thickness of the electrode active layers, the half-thickness of the current collector as electrodes that are single side coated, and the separator

thickness. The overhang from the negative electrode or the separators are not considered, such as the tabs, the electrolyte excess or the coffee bag. Only the essential parts of the electrochemical system are taken into account.

Galvanostatic cycling was carried out in a battery tester (Arbin) with a current rate or C-rate of C/20 for the first 2 cycles until reaching cut-off voltages of 10 mV and 1 V for half-cells. Cycles are then performed with the same cut-off voltages but a C-rate of C/5. For the SLP cells, the first three cycles are performed at C/20, C/10 and C/5 between 2.5 and 4.2 V with a compression set-up applying a constant thickness with an initial pressure of 1 bar. Following cycling is performed at C/3 with check-ups at C/10 after each 20 cycles at C/3 series.

Swelling of the cell thickness was measured using an *operando* compression set-up applying 0.5 MPa on the active surface of the cathode with 3 linear variable differential transformer sensors around the pouch cell as described in our previous reports.[36,37]

LCA methodology

A cradle-to-gate Life Cycle Assessment[38] (LCA) was performed using SimaPro 9.6.0.1 to evaluate the environmental impacts of the innovative GtSi anode and its integration into a laboratory-scale 40 mAh Si–NMC single-layer pouch cell (Fig. S3). The collected inventory relied mainly on laboratory-scale experimental data (primary data) and was complemented with literature when experimental data were not available (secondary data). Background processes were modelled using Ecoinvent v3.9. Lack of primary data and reliance on outdated sources are a major bottleneck in LCAs of batteries, particularly when dealing with novel technologies.[39] Given this, the primary objective of this LCA is to fill data gaps, matching the development of a technology with the collection of the data necessary to build a transparent inventory. The secondary objective is to use this data and the related assessment to determine if there are environmental hotspots already detectable at the laboratory scale, in order to discuss possible early-stage countermeasures. The functional unit (FU) was adopted as "*one 40 mAh Si–NMC single-layer pouch cell*" produced at the laboratory scale. This FU was seen as the most efficient for data collection at the lab scale and for the transparent reporting of data themselves. Such a FU was equally seen as the most meaningful for the interpretation of the current LCA results, as well as the use of inventory data in future LCAs. As the LCA was carried out at the laboratory scale, the results should not be extrapolated beyond this context, as laboratory conditions differ substantially from those of industrial manufacturing and the associated impacts might not be directly comparable with those reported for commercial batteries. The lab-scale synthesis of 1 g of R-GtSi composite was modelled separately to identify the main hotspots of the new process. The impact assessment was carried out using the Environmental Footprint (EF) 3.1 method, consistent with EU guidelines.[40] The discussion focuses on five relevant midpoint indicators:[41] (i) acidification, (ii) climate change, (iii) particulate matter, (iv) resource use fossils, and (v) resource use minerals and metals.

Results and discussion

New *vs.* recycled battery-grade graphite for GtSi

GtSi was synthesized by direct growth of silicon on graphite as Si nanowires (SiNWs), following our previous work[42] (Fig. 1). A thin layer of SnS nanoparticles was first deposited on the graphite as seeds for the catalytic growth of Si. Then the SnS-covered graphite was heated in a pressure reactor in the presence of diphenylsilane (Fig. S2).

Recycled graphite originated from black mass obtained through lithium-ion battery (LIB) recycling by froth floatation. The material was subsequently sent back to EcoGraf and purified using the EcoGraf proprietary purification process, as described in Olutogun *et al.*,[43] where graphite recovered from spent LIBs was recycled for use in new LIBs. The graphite was intensively mixed with caustic soda and heat-treated at approximately 500 °C to evaporate the water content and form a solid cake. The resulting cake was washed in a water bath, allowing the individual particles to detach and form a dispersion. After filtration, the aqueous dispersion was treated with diluted sulfuric acid at moderate temperatures, dissolving sodium-associated impurities into the liquid phase. Following completion of the reaction, the remaining graphite was filtered and thoroughly washed until a neutral pH was achieved.

As a comparison, battery-grade graphite of type SLP30, with a similar morphology and size distribution (Fig. 2a & d), was chosen as a reference material. The elemental analysis by EDX (Table S1) shows the presence of residues of metals in graphite, mainly Ni (0.85%) and Al (0.13%). The specific capacity of recycled graphite in LIBs was found to be lower by a few % than that of new graphite (Fig. S4), respectively 365 *vs.* 412 mAh g^{-1}. The initial coulombic efficiency was also reduced, with values of 80.5% for recycled graphite and 88% for the reference material.

Reaction conditions were optimized to target a Si loading of 20% by weight to attain a GtSi-specific capacity close to 1000 mAh g^{-1}. The nanostructure of GtSi (Fig. 2b and e) shows graphite micro-particles covered with SiNWs of varying diameters (Fig. 2c and f), as typically obtained from Sn-seeded Si growth.[44] The same nanostructure (Fig. S5 & S6) and same Si loadings of 18 to 20% were obtained for n-GtSi and R-GtSi. The specific capacity in delithiation of the GtSi anode materials was

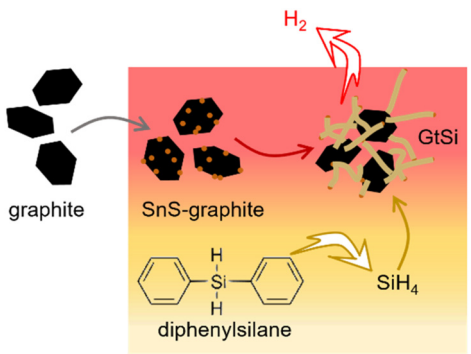

Fig. 1 Scheme of the GtSi synthesis process.

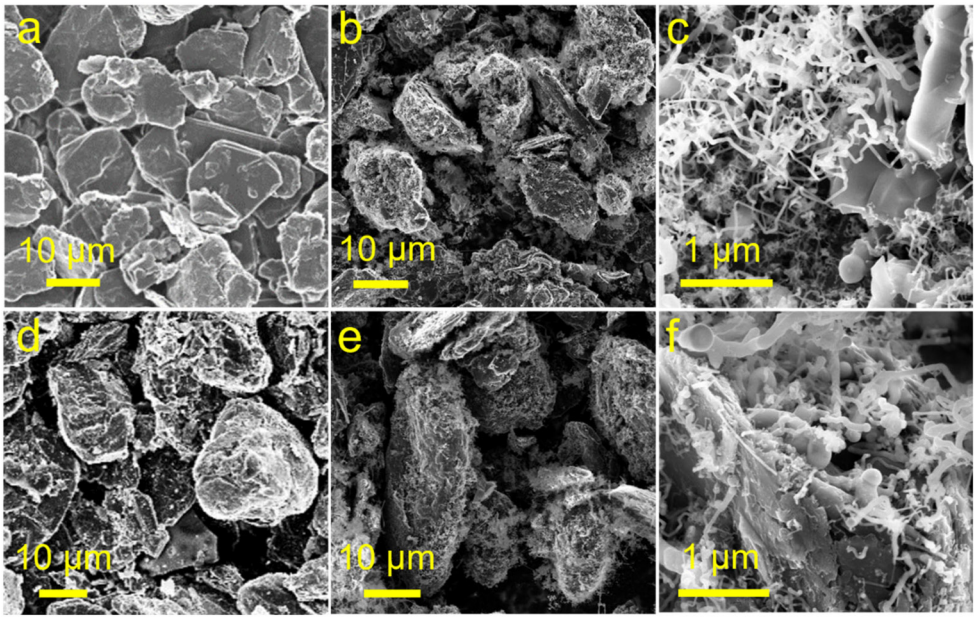

Fig. 2 SEM images of battery-grade (a) and recycled (d) graphite and of n-GtSi (b and c) and R-GtSi (e and f) composites.

measured in half-cell configuration in coin cells at 950 mAh g^{-1} for both n- and R-GtSi (Fig. S7). However, the coulombic efficiency is 88.2% for n-GtSi compared to 84.0% for R-Gt-Si in accordance with the performance of new and recycled graphite.

Safe silicon growth in a compact reactor

As widely described for chemical vapor deposition processes,[45] SiNW growth proceeds *via* a vapor–liquid–solid mechanism: (i) the gaseous silicon source, usually silane SiH_4, decomposes at the surface of a liquid metal droplet (here Sn); (ii) Si dissolves in the seed, releasing hydrogen gas along eqn (1); (iii) Si crystallizes once saturation is attained in the droplet along eqn (2), which induces nanowire growth.

$$SiH_4 + Sn_{liq} \rightarrow Si_{solute\ in\ Sn} + 2H_2 \quad (1)$$

$$Si_{solute\ in\ Sn} \rightarrow Si_{crystal} \quad (2)$$

SiNW growth operated from SiH_4 demands stringent safety measures associated with handling this pyrophoric gas at all stages from shipping to storing in pressurized cylinders, circulating, reacting and discarding. Specific safety assets and procedures dedicated to SiH_4 use have been set for the chemical industry of semiconductor manufacturing, electronics or photovoltaics. In chemistry labs handling many other dangerous chemicals, such highly specific assets are not available. More stable silanes[46] and organosilanes[31,32,47] provide safe surrogates which proved efficient in SiNW growth. Diphenylsilane is particularly attractive because of its safe storage and handling under ambient conditions and its good reactivity[47] above 350 °C. Using diphenylsilane as a SiH_4 surrogate adds several steps in the mechanism. We recently showed that the well-known bimolecular disproportionation[48] of diphenylsilane yielding SiH_4, following eqn (3)–(5), was supplemented by a radical reaction[34] starting with the thermal homolytic breaking of diphenylsilane into a silylene double radical and benzene (eqn (6)), even at 400 °C.

$$2SiPh_2H_2 \Leftrightarrow SiPhH_3 + SiPh_3H \quad (3)$$

$$SiPh_2H_2 + SiPhH_3 \Leftrightarrow SiH_4 + SiPh_3H \quad (4)$$

$$SiPh_3H + SiPhH_3 \Leftrightarrow SiH_4 + SiPh_4 \quad (5)$$

$$SiPh_2H_2 \rightarrow SiPhH + C_6H_6 \quad (6)$$

This decomposition process produces a slow *in situ* release of SiH_4, thereby avoiding the safety requirements associated with shipping, storage and handling of this pyrophoric gas. We developed on this basis a batch process in a closed reactor, under 430 °C at 10–20 bar, to synthesize GtSi composites using first standard gold seeds[19] and then more sustainable SnS seeds.[42] However, since the growth process evolves hydrogen in eqn (1), the growth was limited by the high pressure of this explosive gas, built-in over a few hours in the closed reactor. In order to limit the risk, the reactor was equipped with a spillway (Fig. S2) keeping the internal pressure below 10 bar. With a 300 mL reactor chamber, this amounts to 50 mmol stored H_2 in the pressure chamber (equivalent to 1.2 L at standard pressure and temperature). The gases slowly escaping *via* the spillway are first diluted in a neutral gas and then evacuated with an exhaust towards hood venting.

A water-cooled condenser prevents organosilane vapors from exiting through the exhaust. However, SiH_4 is a gas at room temperature and may escape together with H_2. Since SiH_4 is pyrophoric, there is a significant risk of ignition, producing a bright white flame at the exhaust. Additionally, any escaping SiH_4 represents a loss in the reaction yield. It is thus of prime importance to control the rate of formation of SiH_4

and to fit it with the rate of SiNW growth so that all SiH_4 is consumed in the reaction chamber. Unfortunately, the thermal decomposition of diphenylsilane is little studied and its dynamics is mostly undescribed.

Controlling diphenylsilane pyrolysis

The kinetics of diphenylsilane thermal decomposition was thus studied independently. A constant amount of pure diphenylsilane, phenylsilane or triphenylsilane was sealed in a glass tube under vacuum and heated in a tubular furnace at 300 or 400 °C for different times, and then the composition in SiH_4, $PhSiH_3$, Ph_2SiH_2, Ph_3SiH and Ph_4Si was determined by ^{1}H-NMR (Fig. S1 and Tables S2–S4). The concentration profiles over time were fitted (Fig. S8 and Note S1) with a chemical dynamics model taking into account all phenyl-hydride exchange reactions. Some benzene was detected at 400 °C in a small amount so that the radical pyrolysis pathway of eqn (6) was neglected in a first approximation. The rate and equilibrium constants were determined from the best fit (Table 1).

The rate constants show a consistent increase in temperature of at least a factor of 20 between 300 and 400 °C. A rough estimate by the Arrhenius law gives activation energies of 100 to 120 kJ mol^{-1}, much lower than the C–Si bond energy of 318 kJ mol^{-1}, in line with a concerted reaction pathway for the disproportionation reaction (3), as proposed in the literature.[48–51] A closer look at the forward and reverse rate constants at 400 °C (Table S5) shows that reactions involving hydride release from SiH_4 are slower than from phenylsilanes, indicating that the phenyl moiety stabilizes the transition state. This confirms the better reactivity of arylsilanes than alkylsilanes in thermolysis reported in the literature.[47,51] Inversely, the reactions involving phenyl release from $SiPh_4$ show faster rates, probably due to the relaxation of internal steric hindrance. Interestingly, the equilibrium of hydride-phenyl exchange at 400 °C appears to be displaced towards the production of SiH_4, which allows a good use of phenylsilanes as an *in situ* source of SiH_4. However, making $SiPh_4$ is unfavorable both thermodynamically and kinetically, which reduces the overall yield.

The pressure and temperature record in the reactor gives access to n, the amount of gas in the chamber, produced either by evaporation or by using a chemical reaction. During SiNW growth, the pressure starts rising steadily during the heating ramp from 200 °C (Fig. 3a), then it goes on increasing at the temperature plateau. Since diphenylsilane decomposes only in a few hours at 300 °C as shown above, we attribute the fast pressure rise in the heating ramp to diphenylsilane evaporation. When the temperature reaches the plateau around 400 °C, the net gas production is attributed to simultaneous diphenylsilane pyrolysis and SiNW growth. In the closed SiNW growth reactor, these two successive phases appear as two separate peaks at 0.2 and 0.6 hours in the rate of gas production as a function of time, dn/dt (Fig. 3b). The reaction shows a fast decay, with dn/dt following an apparent power law in t^{α} with α = −1.5 to −2.2 for all records (Fig. 3c).

The reaction yield in the closed reactor is limited by the built-in pressure of hydrogen as a by-product. Switching to a half-open reactor (Fig. 3d & g) allows keeping a safer low inside pressure so that the diphenylsilane loading and reaction time could both be increased by a factor of 5 to 10. An increase in temperature from 350 to 390 °C led to a rather small gain in Si conversion yield from 16% to 20% (Fig. 3e and S9). However, 390 °C was found to be the upper limit because the high gas production rate at the beginning of the reaction induced the escape of SiH_4 as a silica-producing flame through the exhaust. Alternatively, the half-open reactor was operated with a slow temperature ramp from 350 to 435 °C optimized to stabilize the gas production rate dn/dt over several hours (Fig. 3g–i), thus allowing a long SiNW production time without SiH_4 loss.

Interestingly, when operating the half-reactor at constant temperature, the reaction rate during the long temperature and pressure plateau decayed slower than in the closed reactor (Fig. 3e), dn/dt, following an apparent power law in t^{α} with α = −0.8 to −1.1 over several hours (Fig. 3f). This difference in chemical dynamics indicates the detrimental effect of excess hydrogen in the closed reactor. We already reported that the presence of a non-reactive gas like argon can significantly modify the rate of thermal decomposition of diphenylsilane.[44] This effect is probably due to the non-ideality of the reactive gases under growth conditions. A heavy gas with a behavior far from ideality (see Note S2 and Table S6), diphenylsilane, would show a significantly higher vapor pressure under a global pressure of 10 bar (as in the half-open reactor) than at 20 bar (in the closed reactor), thus maintaining a higher availability of the silicon source. Avoiding high hydrogen pressure in the half-open reactor would thus bring an additional advantage in favoring the kinetics of silane production.

Table 1 Equilibrium and rate constants of the reactions of phenyl and hydride exchange between phenylsilane species at 300 and 400 °C

Reactions	Equilibrium constant		Rate constant (L mol^{-1} min^{-1})	
Temperature	300 °C	400 °C	300 °C	400 °C
$2SiPh_2H_2 \Leftrightarrow SiPhH_3 + SiPh_3H$	0.9	0.535	0.02	0.58
$SiPhH_3 + SiPh_2H_2 \Leftrightarrow SiH_4 + SiPh_3H$			0.012	0.26
$SiPhH_3 + SiPh_3H \Leftrightarrow SiH_4 + SiPh_4$			ND	0.19
$2SiPhH_3 \Leftrightarrow SiH_4 + SiPh_2H_2$	0.2	11.8	0.001	0.51
$SiPh_2H_2 + SiPh_3H \Leftrightarrow SiPh_4 + SiPhH_3$			ND	0.27
$2SiPh_3H \Leftrightarrow SiPh_4 + SiPh_2H_2$	ND	0.22	ND	0.033

ND: not determined.

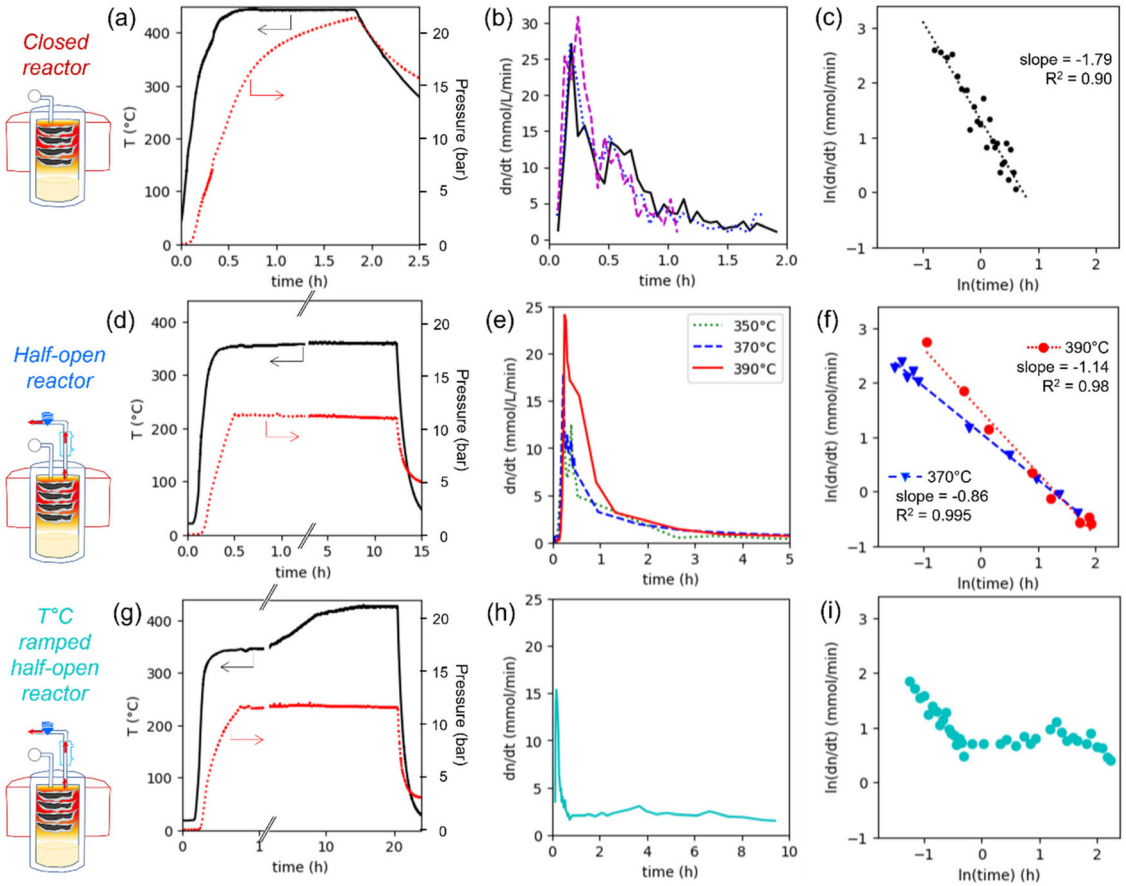

Fig. 3 GtSi growth dynamics in the closed (a–c) and half-open reactor (d–f) at constant temperature and in the half-open reactor under a temperature ramp (g–i). (a, c and g) Temperature and pressure *vs.* time during GtSi synthesis. (b, e and h) Time derivative of the molar quantity of gas, d*n*/d*t*, in the chamber as a function of time *t*, for three equivalent experiments (b) or at different temperatures (e). In (e and h), the reaction rate was measured by temporarily closing a valve to the spillway for 60 s to measure the pressure rise. (c, f and i) Same data as in (b, e and h) on a log–log scale and linear regression lines.

Scaling-up GtSi synthesis on new and recycled graphite

Overall, the gas spillway and the temperature ramp allowed an increase in the amount of silicon and GtSi produced by a factor of 25 (Fig. 4), while increasing the reactor volume only by a factor of 2, thus maintaining a low risk with a constant quantity of stored hydrogen. This very compact process reproducibly yields 5 g of silicon as SiNWs in 25 g of GtSi composite within a chamber of only 300 mL. The process improvement also led to an increase in the yield of conversion of diphenylsilane to 30–35%, close to the maximum theoretical 50% yield for this reaction, following the global eqn (7). The yield seemed to plateau around 35%, a result in line with our kinetics study showing that the formation of $SiPh_4$ is thermodynamically unfavorable (Table 1).

$$2SiPh_2H_2 \rightarrow SiNW + SiPh_4 + 2H_2 \quad (7)$$

The scaled-up process was successfully extended to recycled graphite with a similar yield and mass (Fig. 4 and Fig. S10), with no further optimization required. We inquired whether the metal impurities present in recycled graphite (Table S1) would compete with tin as seeds for the catalysis of diphenylsilane decomposition or SiNW growth. Indeed, the main metal impurities in recycled graphite are Ni and Al, known as efficient seed metals for SiNW growth[52] but at a much higher temperature (>500 °C) than the 350–435 °C implemented here. First, no significant difference was observed in the pressure/temperature/reaction rate profiles for the R-GtSi and n-GtSi synthesis, showing that the decomposition of diphenylsilane was not affected. Second, the SiNW growth in the upscaled conditions produced composites with slightly higher SiNW diameters than in the closed reactor (Fig. S11). However, GtSi composites produced at a large scale from new and recycled graphite showed the same SiNW diameter distribution reproducibly (Fig. S12), and the same Si/Sn mass ratio (Fig. 4). Third, attempts to map Ni or Al by EDX in R-GtSi did not allow spotting Ni- or Al-rich particles at the surface. Ni and Al were only detected at low levels in random areas of the material.

Finally, the X-ray diffraction patterns of R-GtSi and n-GtSi were recorded, refined and compared in detail (Fig. S13). The diffractograms were very similar, showing well defined peaks, among which all fitted in the tabulated patterns of graphite,

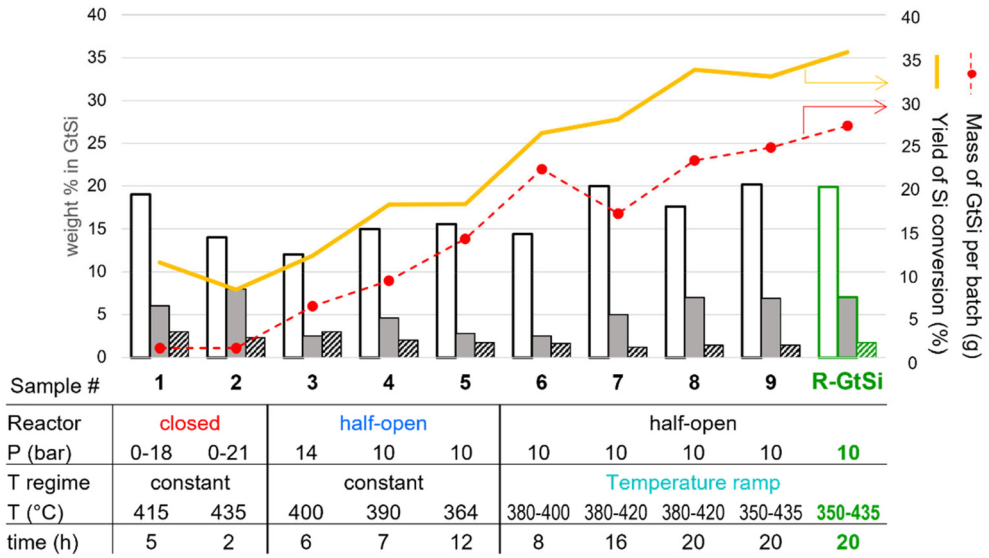

Fig. 4 Improving GtSi mass production (dotted line) and Si conversion yield (continuous line) with reactor design and the optimized temperature regime in a series of 10 syntheses. Samples of n-GtSi are denoted in black and R-GtSi in green. For each product, the bar plot reports the GtSi weight content in Si (empty bar), Sn (grey bar) and O (striped bar), the remaining being C.

silicon or tin. The 7 well separated Si peaks of R-GtSi had a peak width consistently larger by 14% as compared to n-GtSi, probably due to a slight difference in average SiNW size distribution (Fig. S12). The graphite pattern of R-GtSi showed the same (0,1,0) and (1,1,0) reflections as n-GtSi, while all (*h*,*k*,*l*) reflections with a non-zero *l* parameter had a significantly lower intensity. This is consistent with an equal lattice distance as reported earlier,[29] but a slightly increased disorder of graphene layer stacking in the recycled graphite. As for tin, a dozen reflections were observed with a similar intensity and peak width for n- and R-GtSi, indicating no change in the seed phase. As a conclusion, although metal impurities brought by the recycled graphite are clearly present in R-GtSi, they do not produce detectable effects, neither in the reactivity nor in the structure of R-GtSi.

In the scaled-up synthesis, the reaction yield was noticeably limited by the diffusion of reactive gases towards the seeds on the graphite powder surface. This diffusion limitation in porous substrates of more than a few millimeter thickness was already observed in our previous studies,[53] which demonstrated significantly increased SiNW diameters inside the porous matrix as compared to the surface. To limit this effect, the graphite powder was thus spread as <0.5 cm thick layers on a dozen aluminum foil squares (Fig. S2) to favor gas diffusion. The growth yielded blocks of compact GtSi composites in which dense intertwined SiNWs brought cohesion between neighboring graphite grains (Fig. S14). Such limitations are solved at the industrial scale by fluidized bed processes or rolling containers.[54]

Anode roll-to-roll fabrication, LIB assembly and test

With the aim to demonstrate the performance of the GtSi composites in LIBs, thick electrodes were coated in a roll-to-roll coating process with an areal capacity of 4.2 mAh cm^{-2} or a loading of 4.5 mg cm^{-2}. At the cathode side with a high nickel content NMC811 material, the corresponding loading is 21 mg cm^{-2} and the cells have a final balancing of 1.03. The GtSi electrodes were coated with a composite proportion of 90% in the negative electrode formulation and with a width of 7 cm. It also contains 5.8% of binder and 4.2% of 3 different electronic conductive additives for a slurry solid content of 23.5% by weight. The electrodes are suitable at the end of the dryer on the coating machine without any cracks (Fig. 5a). They were pressed down to a thickness of 44 μm to reach a density of 1.35 g cm^{-3} before being assembled in SLP cells. The anode specific capacity is 855 mAh g^{-1} and 1155 mAh L^{-1}, based on the total content of the anode layer (GtSi composite, conductive additives and binder). The volume specific capacity is higher by a factor of 2 compared to a standard graphite anode and 50% higher than the last generation of the silicon-based anode. The performance at the first three cycles with a C-rate increase is presented in Fig. 5b and Fig. S15. The SLP containing the n-GtSi composite shows a significantly higher initial coulombic efficiency of 85.0% in comparison with 80.5% for R-GtSi in accordance with the results in half-cells. The structural irreversibility of the positive electrode is added to the irreversibility associated with the solid-electrolyte interface (SEI) at the negative electrode. The n-GtSi composite SLP demonstrates a higher initial capacity with an energy density of the cell electrochemical core of 984 Wh L^{-1} (see Table S7 for calculation parameters) that decreases during subsequent cycles mostly due to the increased C-rate while the coulombic efficiency increases.

During cycling at C/3 with a check-up at C/10 every 21 cycles, the coulombic efficiency stabilizes at around 98.8 and 98.2% for n-GtSi and R-GtSi composites respectively during

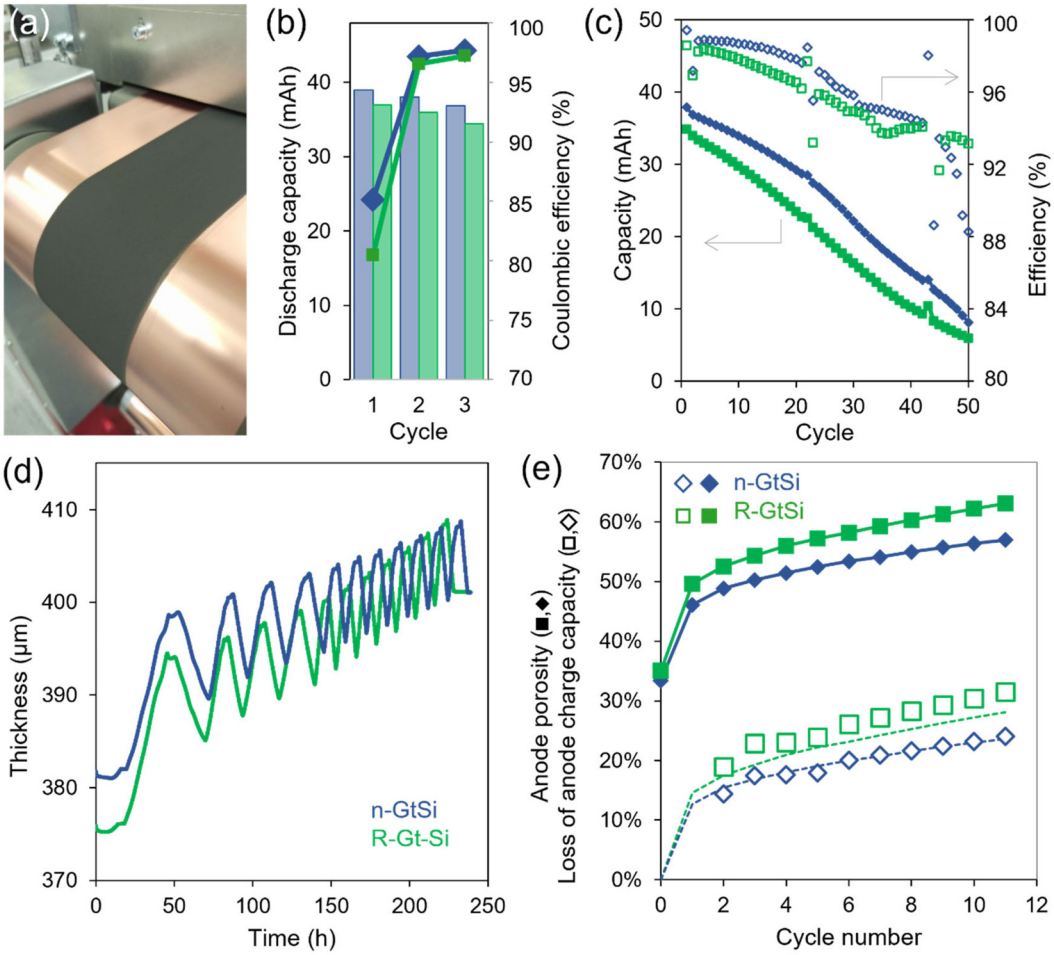

Fig. 5 Electrochemical and mechanical tests in LIBs for n-GtSi (blue diamonds) and R-GtSi (green squares). (a) The R-GtSi electrode at the end of the coating machine. (b and c) Electrochemical evaluation of electrodes in SLP cells (b) during the formation step and (c) during cycling at C/3 with capacity retention (full symbol) and efficiency (open symbol). (d) Swelling of SLP cells during cycling under a constant pressure of 0.5 MPa; (e) corresponding anode porosity in the discharged state (full symbols) and the loss of charge capacity (empty symbols) as a function of cycle number. The dotted lines show the anode porosity increase, after subtraction of the porosity before cycling.

the initial cycles before decreasing (Fig. 5c). The acceleration should be due to the significant swelling of the pouch cell, which was further investigated by *operando* thickness measurement (Fig. 5d) coupled to electrochemistry. The anode porosity was then calculated assuming that cell swelling was due mostly to anode swelling, as is usually the case in silicon-rich cells (Fig. 5e). The fast increase to 57% and 63% porosity for n-GtSi and R-GtSi, respectively, in 11 cycles probably leads to the absorption of the electrolyte, the formation of a new SEI and particle disconnection from the electronic network. Indeed, the percentage loss of charge capacity (empty symbols) correlates remarkably well with the increase in porosity, plotted as dotted lines, for both n-GtSi and R-GtSi electrodes. Our previous work on GtSi composites with thinner SiNWs highlighted the buffering effect brought by graphite,[19] which reduced the Si-rich anode swelling considerably as compared to carbon black-SiNW composites. This volume-change buffering proved less effective with SiNWs of larger diameters[44] as synthesized here, probably because of a lower

Table 2 Inventory data related to the lab-scale assembly of a 40 mAh pouch cell

Si-NMC pouch cell composition	Quantity	Unit
Inputs		
Aluminium collector	0.168	g
NMC811 cathode slurry	0.217	g
Copper collector	0.427	g
R-GtSi anode slurry	0.056	g
Separator	0.013	g
Electrolyte	1	g
Plastics	0.600	g
Aluminium pouch	0.130[a]	g
Electricity	0.059[b]	kWh
Heat	0.001[a]	MJ
Outputs		
Pouch cell	**1**	**Piece**
Solid waste	0.112	g

[a] Secondary data.[58] [b] Secondary data.[57]

inter-nanowire porosity. The significantly higher swelling of R-GtSi as compared to n-GtSi may indicate that recycled graphite has a lower ability to absorb mechanical pressure, possibly due to a lower or filled internal porosity. While the composite electrodes present huge volume capacity associated with a suitable initial coulombic efficiency, the high specific surface of the nanostructure probably induces the low coulombic efficiency upon cycling. A coating to embed the silicon nanowires and a more effective binder to absorb the mechanical constraints, as reported for other GtSi materials in the literature,[5,17,55] should be an efficient way to achieve long capacity retention.

Table 3 Inventory data related to the lab-scale synthesis of 1 g of GtSi composite with recycled graphite

R-GtSi composite	Quantity	Unit
Inputs		
Catalyst (SnO_2)	0.08	g
Recycled graphite	0.8	g
SiH_4	0.38	g
Electricity	0.22	kWh
Outputs		
R-GtSi	**1**	**g**
Solid waste	0.18	g
H_2	0.0284	g

Life cycle analysis

Life cycle inventory data for 40 mAh single-layer pouch cell production and for R-GtSi synthesis are reported in Tables 2 and 3, respectively. Since no dataset for $SiPh_2H_2$ was available in Ecoinvent and the related inventory could not be modelled from primary or literature data, silane (SiH_4, also known as silicon tetrahydride) was used as a proxy, as it represents a similar silicon precursor. This proxy seems adequate since many industrial processes for nano-silicon synthesis (by Nanomakers, France, OneD and Amprius, USA) rely or have long relied on silane as a precursor. Data for recycled graphite were adapted from Rey *et al.*,[56] describing a leaching and filtration recovery route from spent LIB anodes. The unit process representing the mixing and feeding of electrolytes (DMC, EMC, EC, $LiPF_6$, and some additives) was adapted from Chordia *et al.*[57] Electricity use was modelled using the European grid mix, reflecting the laboratory location. The energy demand for cell assembly was adapted from industrial LIB data, assuming similar processing steps. The small amount of solid residue was modelled as non-hazardous waste.

The cradle-to-gate environmental impacts associated with the production of the pouch cell and the synthesis of R-GtSi composites are shown in Table 4. Fig. 6 presents the contribution analysis, according to which the copper current collec-

Table 4 Environmental indicators related to the synthesis of 1 g of R-GtSi composite and the production of a Si-NMC pouch cell at the lab-scale

Environmental indicator	Si-NMC pouch cell	1 g of R-GtSi	Unit
Acidification	5.36×10^{-4}	1.82×10^{-3}	mol H^+ eq.
Climate change	5.07×10^{-2}	3.84×10^{-1}	kg CO_2 eq.
Particulate matter	2.61×10^{-9}	1.41×10^{-8}	Disease inc.
Resource-use and fossils	8.96×10^{-1}	5.70	MJ
Resource-use, minerals and metals	3.96×10^{-6}	2.15×10^{-6}	kg Sb eq.

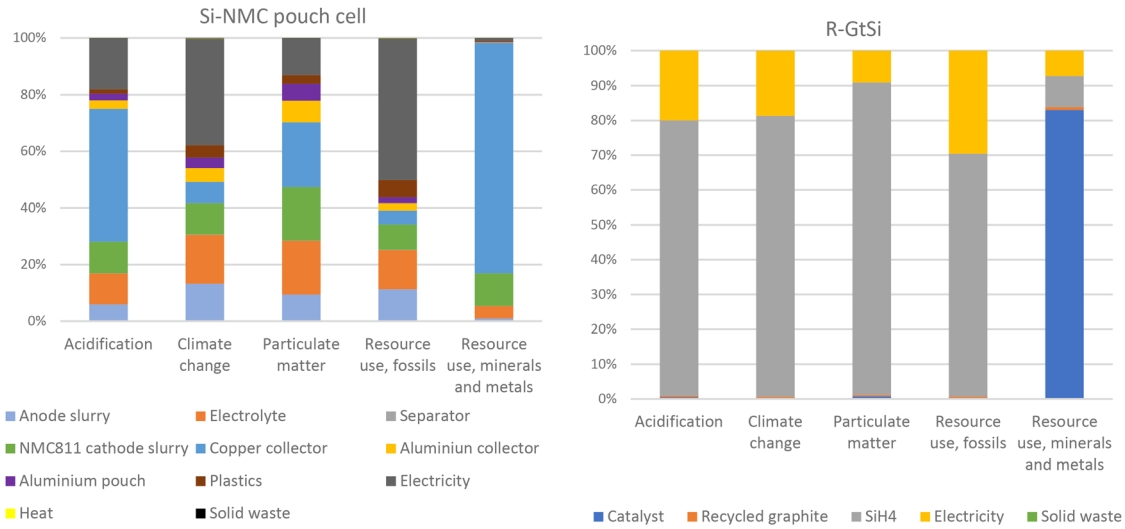

Fig. 6 Contribution analysis related to the cradle-to-gate LCA of a Si-NMC pouch cell (left) production and 1 g of R-GtSi composite synthesis (right) at the lab-scale.

tor accounts for 47% of acidification and 81% of resource use, minerals and metals, mainly due to the energy- and emission-intensive processes involved in copper extraction and refining, while electricity consumption dominates climate change (38%) and resource use and fossils (50%). The electrolyte also shows a significant contribution, although this is likely overestimated due to the non-optimized quantities typical of lab-scale assembly.

After identifying the main contributors at the cell level, the analysis concentrated on the R-GtSi composite synthesis. The GtSi-based anode is a minor contributor to the overall cell impacts, yet the GtSi synthesis process (Fig. 6) highlights a significant contribution to the composite impacts from SiH_4 (over 70% in all categories except for resource use, minerals and metals) and electricity consumption, reflecting the energy-intensive nature of silane production and the low process efficiency typical of laboratory-scale operations. These impacts could be reduced through materials and energy optimization and the use of Si waste from the photovoltaic industry for direct SiNW growth.[4] Reduced silicon could not be directly recycled from spent LIBs due to its transformation into an ultra-porous foam during cycling.[59] However, recycled sources of reduced silicon are now more available from the dismantling of end-of-life solar panels.[60] Several teams already reported turning solar panel Si into nanoparticles[61–63] or nanowires[4] for LIBs, although the energy consumption must still be improved. Alternatively, recycled Si could be used instead of metallurgical Si for the synthesis of silane reagents with a lower environmental impact. The catalyst mainly drives resource use, minerals and metals, while the recycled graphite shows minor impacts.

Conclusion

This study demonstrates the feasibility and relevance of upgrading recycled graphite into high-performance GtSi anodes using scalable and industrially relevant processes. The roll-to-roll battery fabrication and test reported in this paper highlighted the very high energy density that could be obtained with GtSi composites derived from recycled graphite, coupled with a remarkably low irreversible capacity in the first cycle. Through optimized binder formulations and conductive additive selection, the GtSi anodes achieved a volumetric capacity of 1150 Ah L^{-1}, corresponding to a twofold increase relative to conventional graphite anodes while remaining compatible with practical areal capacities. Although long-term capacity fading can be mitigated using surface coatings such as carbon or titanium oxide, as reported in the literature, these strategies were beyond the scope of the present study. However, the high reliability of these scaled-up battery tests enabled the identification of a small but systematic difference in cycling stability between recycled- and new-graphite-based GtSi. In-depth analysis of the behavior of the cell and its compounds led to the conclusion that the main cause of this faster decay was uncompensated anode swelling due to silicon volume changes during cycling. We hypothesize that recycled graphite presents lower available internal porosity than new graphite and thus a lower ability to buffer silicon swelling.

Beyond electrochemical performance, the scale-up of the GtSi synthesis offered opportunities for both a safety analysis of gram scale silicon growth and a life-cycle analysis of nano-silicon manufacturing. Diphenylsilane, as a surrogate for silane SiH_4 *via in situ* thermal decomposition, is demonstrated here to be a safe reagent for growing large quantities of silicon, provided the risks associated with H_2 evolution, together with traces of pyrophoric silane or organosilane vapors, are carefully assessed. The kinetic and thermodynamic parameters reported here offer a quantitative basis for predicting reaction behavior and defining safe operating windows for any phenylsilane- or diphenylsilane-based reaction processes.

Clear and transparent life cycle inventories for R-GtSi composites and pouch cell production at the lab scale have been presented, which address the need for filling data gaps in LCIs and LCAs in the battery field. Looking at the LCIA results, the main contributors to the pouch cell's impacts are electricity consumption and the copper collector. Meanwhile, the life cycle analysis of the reported R-GtSi composite identifies SiH_4 as the main contributor, which stems directly from the high thermodynamic cost associated with Si reduction. Taken together, these results highlight the potential of combining material recycling, scalable silicon growth, and realistic cell-level validation. Overall, this work establishes recycled-graphite-based GtSi as a technically viable and scalable anode material, helping bridge the gap between laboratory innovation and industrial battery manufacturing.

Author contributions

Conceptualization & funding acquisition: GAB, AM, WP and PC; data curation: DDK, AM, WP, and PC; investigation: DDK, TB, MR and PC (silicon growth), DDK and LV (batteries), AV (graphite recycling), and GP (life cycle analysis); supervision: GAB, WP, and PC; writing – original draft: PC, WP, and GP; and writing – review & editing: PC, WP, TB, AM, and AV.

Conflicts of interest

There are no conflicts of interest to declare.

Data availability

The supporting data have been provided as part of the supplementary information (SI). Supplementary information is available. See DOI: https://doi.org/10.1039/d6eb00002a.

For further experimental details, see https://doi.org/10.5281/zenodo.18163142.

Acknowledgements

PC thanks Pierre-Alain Bayle for his support in the design of quantitative ^{1}H-NMR measurements and Sandrine Schlutig and Sabatino Pecoraro for XRD analysis and refinement. This work was carried out with the support of the 2BoSS (Toward sustainable batteries based on silicon, sulfur and biomass derived carbon) project under the ERA-MIN3 program: French grant number ANR-22-MIN3-000301 from Agence Nationale de la Recherche and MUR grant number DELIBERA MUR: N. 0000462, 17/11/2022. We would also like to thank Christoph Frey, Michael Chan, and Andrew Spinks of the EcoGraf team for purifying the recycled graphite sample used in this study.

References

1 M. Armand, P. Axmann, D. Bresser, M. Copley, K. Edström, C. Ekberg, D. Guyomard, B. Lestriez, P. Novák, M. Petranikova, W. Porcher, S. Trabesinger, M. Wohlfahrt-Mehrens and H. Zhang, *J. Power Sources*, 2020, **479**, 228708.
2 J. I. Preimesberger, F. L. E. Usseglio-Viretta, A. Verma, A. Singh, A. M. Colclasure, P. Walker, G. Teeter, G. F. Pach, J. Westgard, F. Urias-Cordero, N. R. Neale, J. E. Coyle and G. M. Carroll, *EES Batteries*, 2025, **1**, 298–309.
3 Y. K. Jeong, W. Huang, R. A. Vilá, W. Huang, J. Wang, S. C. Kim, Y. S. Kim, J. Zhao and Y. Cui, *Adv. Energy Mater.*, 2020, **10**, 2002108.
4 J. Lu, S. Liu, J. Liu, G. Qian, D. Wang, X. Gong, Y. Deng, Y. Chen and Z. Wang, *Adv. Energy Mater.*, 2021, **11**, 2102103.
5 J. Zhang, D. Wang, R. Yuan, X. Li, J. Li, Z. Jiang, A. Li, X. Chen and H. Song, *Small*, 2023, **19**, 2207167.
6 Y. Chen, L. Liu, J. Xiong, T. Yang, Y. Qin and C. Yan, *Adv. Funct. Mater.*, 2015, **25**, 6701–6709.
7 W. Wang and P. N. Kumta, *ACS Nano*, 2010, **4**, 2233–2241.
8 Z. Xie, W. Zhang, X. He, Z. Gao, Z. Du, H. Yang, X. Zhang, R. Li, Y. He, L. Peng and F. Kang, *Energy Storage Mater.*, 2025, **75**, 104046.
9 Z. Hao, J. Chen, L. Yuan, Q. Bing, J. Liu, W. Chen, Z. Li, F. R. Wang and Y. Huang, *Small*, 2019, **15**, 1902377.
10 D. H. S. Tan, Y.-T. Chen, H. Yang, W. Bao, B. Sreenarayanan, J.-M. Doux, W. Li, B. Lu, S.-Y. Ham, B. Sayahpour, J. Scharf, E. A. Wu, G. Deysher, H. E. Han, H. J. Hah, H. Jeong, J. B. Lee, Z. Chen and Y. S. Meng, *Science*, 2021, **373**, 1494–1499.
11 H. Pan, L. Wang, Y. Shi, C. Sheng, S. Yang, P. He and H. Zhou, *Nat. Commun.*, 2024, **15**, 2263.
12 C. Li, Y. Wu, F. Ren, J. Liu, Y. Lin, M. Xia, H. Wang, C. Meng, Z. Wang, Z. Gong and Y. Yang, *Small*, 2025, **n/a**, 2411451.
13 M. Grandjean, M. Perrey, X. Randrema, J. Laurier, P. Chenevier, C. Haon and S. Liatard, *J. Power Sources*, 2023, **585**, 233646.
14 Q. Shen, R. Zheng, Y. Lv, Y. Lou, L. Shi and S. Yuan, *Batteries Supercaps*, 2022, e202200186.
15 Y.-R. Lee, S. C. Hong, K. Kim, J. Park, J. Kim, B. Kang, Y. Kim, C. Lee, S. Son, B. Cho, J. Kim, S.-G. Woo, G.-H. Lee and K. Kang, *Adv. Energy Mater.*, 2025, e04250.
16 W. Lai, J. H. Lee, L. Shi, Y. Liu, Y. Pu, Y. K. Ong, C. Limpo, T. Xiong, Y. Rao, C. H. Sow and B. Özyilmaz, *J. Energy Chem.*, 2024, **93**, 253–263.
17 S. Jayasubramaniyan, Y. Lee, J. Kim, S. Kim, D. Kim, M. Ko, N. S. Reddy, S. Y. Nam and J. Sung, *Energy Fuels*, 2024, **38**, 18026–18034.
18 I. Profatilova, E. De Vito, S. Genies, C. Vincens, E. Gutel, O. Fanget, A. Martin, M. Chandesris, M. Tulodziecki and W. Porcher, *ACS Appl. Energy Mater.*, 2020, **3**, 11873–11885.
19 S. Karuppiah, C. Keller, P. Kumar, P.-H. Jouneau, D. Aldakov, J.-B. Ducros, G. Lapertot, P. Chenevier and C. Haon, *ACS Nano*, 2020, **14**, 12006–12015.
20 C. L. Berhaut, D. Z. Dominguez, D. Tomasi, C. Vincens, C. Haon, Y. Reynier, W. Porcher, N. Boudet, N. Blanc, G. A. Chahine, S. Tardif, S. Pouget and S. Lyonnard, *Energy Storage Mater.*, 2020, **29**, 190–197.
21 J. M. Hartley, S. Scott, J. M. Yang, P. A. Anderson, G. D. J. Harper, J. Ahuja, E. Petavratzi, H. Tulsidas and A. P. Abbott, *EES Batteries*, 2025, **1**, 1502–1514.
22 A. Miswanto, T. Wahyudi, A. Prakosa and D. C. Birawidha, *Indonesian Mining Journal*, 2023, **26**, 93–106.
23 A. Vanderbruggen, J. Sygusch, M. Rudolph and R. Serna-Guerrero, *Colloids Surf., A*, 2021, **626**, 127111.
24 J. Park, S.-J. Cho, S. Shin, R. Kim, D. Shin and Y. Shin, *Geosci. J.*, 2025, **29**, 329–341.
25 L. Kutscher, E. Notté and K. Anderson, *Green Health*, 2025, **1**, 14.
26 M. Nopeia, M. Deus, L. Vasconcelos and B. J. Malumuge, *Extr. Ind. Soc.*, 2026, **25**, 101807.
27 A. Manzini, L. Martinez García and P. Harrivaara, *Miner. Econ.*, 2026, **39**, 71–91, DOI: 10.1007/s13563-025-00492-z.
28 M. Olutogun, A. Vanderbruggen, C. Frey, M. Rudolph, D. Bresser and S. Passerini, *Carbon Energy*, 2024, **6**, e483.
29 Z. Yao, X. Ma, R. Wang, J. Hou, J. Fu, Z. Meng, P. Thanwisai, Z. Yang and Y. Wang, *J. Power Sources*, 2025, **625**, 235738.
30 O. Burchak, C. Keller, G. Lapertot, M. Salaün, J. Danet, Y. Chen, N. Bendiab, B. Pépin-Donat, C. Lombard, J. Faure-Vincent, A. Vignon, D. Aradilla, P. Reiss and P. Chenevier, *Nanoscale*, 2019, **11**, 22504–22514.
31 G. Flynn, K. Stokes and K. M. Ryan, *Chem. Commun.*, 2018, **54**, 5728–5731.
32 A. T. Heitsch, D. D. Fanfair, H.-Y. Tuan and B. A. Korgel, *J. Am. Chem. Soc.*, 2008, **130**, 5436.
33 J. C. Chan, H. Tran, J. W. Pattison and S. B. Rananavare, *Solid-State Electron.*, 2010, **54**, 1185–1191.
34 J. Wang, C. Keller, M. Dietrich, P. E. Olli, P. Gentile, S. Pouget, H. Okuno, M. Boutghatin, Y. Pennec, V. Reita, D. N. Nguyen, H. Johnson, A. Morozan, V. Artero and P. Chenevier, *Sustainable Energy Fuels*, 2023, **7**, 4864–4876.
35 J. Zhu, Y. Li and G. Hu, *Ionics*, 2018, **24**, 1265–1269.
36 D. Vidal, C. Leys, B. Mathieu, N. Guillet, V. Vidal, D. Borschneck, P. Chaurand, S. Genies, E. De Vito,

M. Tulodziecki and W. Porcher, *J. Power Sources*, 2021, **514**, 230552.
37 D. Vidal, S. Genies, E. De Vito, M. Tulodziecki and W. Porcher, *J. Energy Storage*, 2023, **64**, 107174.
38 Standard ISO 14040-14044, 2006.
39 M. Erakca, S. Pinto Bautista, S. Moghaddas, M. Baumann, W. Bauer, L. Leuthner and M. Weil, *J. Cleaner Prod.*, 2023, **384**, 135510.
40 Council of the European Union, European Parliament, *Official Journal of the European Union*, 2023, https://eur-lex.europa.eu/eli/reg/2023/1542/oj/eng.
41 The Advanced Rechargeable & Lithium Batteries Association, *PEFCR - Product Environmental Footprint Category Rules for High Specific Energy Rechargeable Batteries for Mobile Applications*, 2020.
42 C. Keller, S. Karuppiah, M. Raaen, J. Wang, P. Perrenot, D. Aldakov, P. Reiss, C. Haon and P. Chenevier, *ACS Appl. Energy Mater.*, 2023, **6**, 5249–5258.
43 M. Olutogun, A. Vanderbruggen, C. Frey, M. Rudolph, D. Bresser and S. Passerini, *Carbon Energy*, 2024, **6**, e483.
44 C. Keller, Y. Djezzar, J. Wang, S. Karuppiah, G. Lapertot, C. Haon and P. Chenevier, *Nanomaterials*, 2022, **12**, 2601.
45 V. Schmidt, J. V. Wittemann and U. Gösele, *Chem. Rev.*, 2010, **110**, 361–388.
46 A. T. Heitsch, V. A. Akhavan and B. A. Korgel, *Chem. Mater.*, 2011, **23**, 2697–2699.
47 D. C. Lee, T. Hanrath and B. A. Korgel, *Angew. Chem., Int. Ed.*, 2005, **44**, 3573–3577.
48 H. Gilman and D. H. Miles, *J. Org. Chem.*, 1958, **23**, 326–328.
49 G. A. Russell, *J. Am. Chem. Soc.*, 1959, **81**, 4815–4825.
50 J. L. Speier and R. E. Zimmerman, *J. Am. Chem. Soc.*, 1955, **77**, 6395–6396.
51 H.-Y. Tuan and B. A. Korgel, *Chem. Mater.*, 2008, **20**, 1239–1241.
52 B. T. Richards, B. Gaskey, B. D. A. Levin, K. Whitham, D. Muller and T. Hanrath, *J. Mater. Chem. C*, 2014, **2**, 1869.
53 C. Keller, A. Desrues, S. Karuppiah, E. Martin, J. P. Alper, F. Boismain, C. Villevieille, N. Herlin-Boime, C. Haon and P. Chenevier, *Nanomaterials*, 2021, **11**, 307.
54 Y. Zhu, J. L. Goldman, J. Hartlove and H. J. Hofler, US11233240B2, EP10778339, 2019.
55 Y.-J. Lee, W.-J. Song, Y.-H. Jo, H.-J. Lee, Y. Kim, G. Im and D.-W. Kim, *ACS Appl. Mater. Interfaces*, 2025, **17**, 57114–57123.
56 I. Rey, C. Vallejo, G. Santiago, M. Iturrondobeitia and E. Lizundia, *ACS Sustainable Chem. Eng.*, 2021, **9**, 14488–14501.
57 M. Chordia, A. Nordelöf and L. A.-W. Ellingsen, *Int. J. Life Cycle Assess.*, 2021, **26**, 2024–2039.
58 S. Wickerts, R. Arvidsson, A. Nordelöf, M. Svanström and P. Johansson, *ACS Sustainable Chem. Eng.*, 2023, **11**, 9553–9563.
59 S. Imtiaz, I. S. Amiinu, D. Storan, N. Kapuria, H. Geaney, T. Kennedy and K. M. Ryan, *Adv. Mater.*, 2021, 2105917.
60 B. Jung, J. Park, D. Seo and N. Park, *ACS Sustainable Chem. Eng.*, 2016, **4**, 4079–4083.
61 Y. Jin, S. Zhang, B. Zhu, Y. Tan, X. Hu, L. Zong and J. Zhu, *Nano Lett.*, 2015, **15**, 7742–7747.
62 B. Sreenarayanan, M. Vicencio, S. Bai, B. Lu, O. Mao, S. Adireddy, W. Bao and Y. S. Meng, *J. Power Sources*, 2023, **578**, 233245.
63 N. Eshraghi, L. Berardo, A. Schrijnemakers, V. Delaval, M. Shaibani, M. Majumder, R. Cloots, B. Vertruyen, F. Boschini and A. Mahmoud, *ACS Sustainable Chem. Eng.*, 2020, **8**, 5868–5879.